



POLITECNICO
MILANO 1863

[RE.PUBLIC@POLIMI](#)

Research Publications at Politecnico di Milano

Post-Print

This is the accepted version of:

Z.F. Luo, F. Topputo

Capability of Satellite-Aided Ballistic Capture

Communications in Nonlinear Science and Numerical Simulation, Vol. 48, 2017, p. 211-223

doi:10.1016/j.cnsns.2016.12.021

The final publication is available at <https://doi.org/10.1016/j.cnsns.2016.12.021>

Access to the published version may require subscription.

When citing this work, cite the original published paper.

© 2017. This manuscript version is made available under the CC-BY-NC-ND 4.0 license

<http://creativecommons.org/licenses/by-nc-nd/4.0/>

Permanent link to this version

<http://hdl.handle.net/11311/1007279>

Capability of Satellite-Aided Ballistic Capture

Z.-F. Luo^{a,b}, F. Topputo^{c,*}

^a*College of Aerospace Science and Engineering, National University of Defense Technology, 410073, Changsha, P. R. China*

^b*Naval Aeronautical and Astronautical University, 264001 Yantai, P. R. China*

^c*Department of Aerospace Science and Technology, Politecnico di Milano, Via La Masa, 34, 20156, Milano, Italy*

Abstract

In this paper we study a special instance of ballistic capture dynamics: the case **in which** the capture orbit about a planet experiences a close passage **to** one or more of its natural satellites. The capability of the satellites in improving ballistic capture is assessed. The dynamical framework considers **at least** the gravitational attractions of the Sun, the planet, and its satellites, all acting on a massless particle. The effect of the satellites is introduced explicitly by modifying a previously developed method, which relies on three-dimensional stable sets and n -body dynamics with precise ephemeris. Once a stability criterium is defined, initial conditions defined over a computational grid are integrated forward and backward. This allows us **to classify** orbits into different sets. Ballistic capture orbits with prescribed features are generated by **manipulating** these sets. Two indices, namely the hyperbolic velocity and the stability index, are used to assess the performance of pre- and post-capture portions, respectively. A Pareto frontier is used to extract orbits of practical interest. Case studies are performed in the context of Earth and Jupiter environments. Comparing to the situation with no moons, the satellite-aided ballistic capture can evidently increase the pre-capture energy and post-capture stability, so making it possible to have permanent capture of a particle at zero-cost. This is a desirable feature in mission design.

Keywords: Ballistic Capture, Stable Sets, Restricted n -Body Problem

*Corresponding author

Email addresses: luozongfu200@nudt.edu.cn (Z.-F. Luo), francesco.topputo@polimi.it (F. Topputo)

1. Introduction

Ballistic capture is a mechanism in which a particle initially in hyperbolic state with respect to a primary can perform a number of revolutions about it in a totally natural way. By definition, this dynamics can be reproduced in restricted n -body models, with $n \geq 3$. Ballistic capture is used in celestial mechanics to study the formation and evolution of the Solar System (Brunini, 1996; Astakhov et al., 2003), the impact dynamics (Benner and McKinnon, 1995; Alessi et al., 2012), and the chaotic exchange of solid material between planetary systems (Belbruno et al., 2012). Ballistic capture is also used in astrodynamics to reduce propellant consumption (Belbruno and Miller, 1993), mitigate the risks associated to single-point burns (Jehn et al., 2004), and accommodate launch window extensions (Topputo and Belbruno, 2015). These features are achieved at the cost of a generally longer transfer time (Circi and Teofilatto, 2001; Ivashkin, 2002).

Ballistic capture orbits are generated with direct numerical simulation due to the lack of analytical solutions. Much effort has been put to view ballistic capture dynamics under the perspective of dynamical system theory in either the circular restricted three-body problem or one of its variants (Conley, 1968; Yamato and Spencer, 2004; Russell and Lam, 2007; Parker and Born, 2008; Mingotti et al., 2012a,b; Ren and Shan, 2014). If, on the one hand, this approach allows us to relate ballistic capture to Lagrange point dynamics, on the other hand, it can be barely adapted in the real model where, e.g., fourth-body perturbations and primaries orbital eccentricity have to be considered. An alternative way to generate ballistic capture orbits consists in computing and manipulating the stable sets of initial conditions, which are associated to a simple, geometrical definition of stability (Belbruno, 2004; García and Gómez, 2007; Topputo and Belbruno, 2009; Sousa Silva and Terra, 2012). Stable sets can be readily computed in the elliptic problem (Hyeraci and Topputo, 2010; Makó et al., 2010; Hyeraci and Topputo, 2013) or in models that attempt to adhere to the real Solar System dynamics (Romagnoli and Circi, 2009; Luo et al., 2014; Brasil et al., 2015). Ballistic capture orbits can be reproduced in these models by manipulation of stable and unstable sets (Luo and Topputo, 2015).

Recent interests in Giant Planets exploration¹ and asteroid retrieval missions² raise the question of a possible use of ballistic capture in such applications. If so, to what extent natural satellites can be exploited to improve capture performances?

¹<http://www.nasa.gov/topics/solarsystem/features/20090218.html> (visited 11 April 2016).

²http://www.nasa.gov/mission_pages/asteroidroids/initiative/index.html (visited 11 April 2016).

In **Solar System** exploration, using Giant Planets’ moons may help both reducing orbit injection costs and mitigating the risks of a single-point **impulsive injection maneuver**. In asteroid retrieval missions, exploiting the Moon can lead to long-term, quasi-stable orbits about the Earth. This argument builds upon previous studies that considered natural satellites to improve trajectory performances (Cline, 1979; Macdonald and McInnes, 2005; Landau et al., 2010; Kloster et al., 2011; Lynam et al., 2011; Campagnola et al., 2014).

In this paper, we elaborate on ballistic capture orbits that experience close encounters with planet’s natural satellites. A previously developed method (Luo et al., 2014; Luo and Topputo, 2015) has been modified to explicitly account for the presence of the moons. The aim is to find orbits having the best balance between pre-capture hyperbolic excess velocity and post-capture stability index. Ideally, this means finding orbits behaving like hyperbolas before the capture, and ellipses afterwards. This dramatic change is sought on a zero cost basis. It is expected that improvements in the post-capture orbit can be obtained when comparing to the simple restricted three-body problem (Kary and Dones, 1996; Tsui, 2000; Astakhov et al., 2003). The analyses are tailored to the case of capture at Jupiter and the Earth. The scopes of the paper are then 1) to modify the existing method to explicitly exploit the presence of the moons, 2) to assess the role played by the moons by using suitable metrics, 3) to compare the results to the case of no aid by the moons in two different scenarios.

The remainder is organized as follows. Section 2 summarizes the reference frames, equations of motion, and numerical techniques used. Section 3 presents the method developed for constructing and ranking ballistic capture orbits. Case studies are given in Section 4. Some **underlying** conclusions are drawn in Section 5.

2. Problem formulations

We study the motion of a particle, a rock or a spacecraft, subject to the gravitation attractions of the Sun, a planet, and its main moons. The planet, of mass m_p , is the body around which the ballistic capture is studied. The Sun–planet mass ratio is $\mu_p = m_p/(m_s + m_p)$, m_s being the mass of the Sun. The analysis is specialized to the case of ballistic capture at the Earth and Jupiter, and thus the Moon as well as the four Galilean satellites are modelled. The planet-moon mass ratio is $\mu_m = m_m/(m_p + m_m)$, where m_m is the mass of the moon considered. The physical parameters used are reported in Table 1.

2.1. Reference frames

The precise locations of the main Solar System bodies at given epoch are retrieved from the JPL planet ephemeris DE430 model. The position vectors are given in the

Table 1: Physical parameters of planets and their natural satellites considered; Gm : gravitational parameter, R : mean equatorial radius, a : semi-major axis, e : eccentricity, T : period, $\mu_{p,m}$: Sun-planet, planet-moon mass ratio, R_s : radius of the sphere of influence (SOI), i : obliquity.

Body	$Gm_{p,m}$ (km^3/s^2)	R (km)	a (km)	e (-)	T (days)	$\mu_{p,m}$ (-)	R_s ($\times R$)	i (deg)
Earth	3.986×10^5	6,371.0	1.496×10^8	0.0167	365.3	3.003×10^{-6}	145.03	–
Moon	4.903×10^3	1,737.4	3.844×10^5	0.0549	27.32	1.215×10^{-2}	38.03	5.15
Jupiter	1.267×10^8	69,911	7.784×10^8	0.0484	4,333	9.537×10^{-4}	674.20	–
Io	5.960×10^3	1,821.5	4.218×10^5	0.0040	1.77	4.704×10^{-5}	4.28	3.15
Europa	3.203×10^3	1,560.8	6.711×10^5	0.0101	3.55	2.528×10^{-5}	6.22	3.58
Ganymede	9.888×10^3	2,631.2	1.070×10^6	0.0015	7.15	7.804×10^{-5}	9.25	3.17
Callisto	7.179×10^3	2,410.3	1.883×10^6	0.0070	16.69	5.667×10^{-5}	15.63	2.90

Earth mean equator and equinox of J2000 (EME2000) and converted into a frame more suitable for our analysis: the planetocentric radial-tangential-normal at epoch t_0 , RTN@ t_0 . In this frame, the z_r -axis is perpendicular to plane of the Sun orbit, the x_r -axis is aligned with the Sun-planet line and points from the Sun to the planet, and the y_r -axis completes the dextral orthonormal triad (see Fig. 1). The transformation from RTN@ t_0 to EME2000 can be found in Luo and Topputo (2015).

The initial conditions are given in RTN@ t_0 and flown under the n -body dynamics. The resulting orbits are also viewed into a barycentric pulsating rotating (BPR) frame, where the x -axis is directed from the Sun to the planet (both at rest on the x -axis), the z -axis is aligned with their orbital angular momentum, and the y -axis completes the triad; the origin is at Sun-planet barycenter. Analyses into the BPR frame are performed on an ex post facto basis.

2.2. Equations of motion

A three-dimensional model for the dynamics is constructed. All the celestial bodies are assumed as being point masses. In the RTN@ t_0 frame the planet is located at the origin, whereas the Sun and the satellites are assumed as revolving in elliptic orbits. Thus, a spatial elliptic restricted n -body problem is formulated with $n = 3 + n_s$, where n_s is the number of moons considered. The Sun and the satellites have phase angles θ_s and θ_k ($k = 1, \dots, n_s$), respectively; see Fig. 1. At the initial epoch, t_0 , these angles are $\theta_{s,0} = \pi$ (by definition) and $\theta_{k,0}$, respectively.

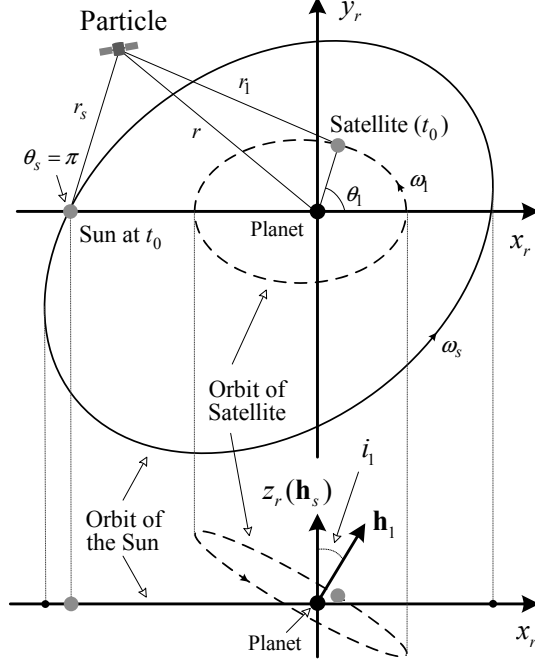


Figure 1: Geometry of spatial elliptic restricted n -body problem used (only one moon shown).

The equations of motion for the massless particle are

$$\ddot{\mathbf{r}} + \frac{Gm_p}{r^3}\mathbf{r} = - \underbrace{Gm_s \left(\frac{\mathbf{r}_s}{r_s^3} + \frac{\mathbf{r} - \mathbf{r}_s}{\|\mathbf{r} - \mathbf{r}_s\|^3} \right)}_{\text{Perturbing from Sun}} - \underbrace{\sum_{k=1}^{n_s} Gm_k \left(\frac{\mathbf{r}_k}{r_k^3} + \frac{\mathbf{r} - \mathbf{r}_k}{\|\mathbf{r} - \mathbf{r}_k\|^3} \right)}_{\text{Perturbing from satellites}}, \quad (1)$$

where \mathbf{r} , \mathbf{r}_s , and \mathbf{r}_k are the spacecraft position vectors with respect to the planet, the Sun, and the satellites, respectively, **whereas** r , r_s , and r_k are their **norms**; Gm are the gravitational parameters. In the elliptic model assumed, the motion of both the Sun and the satellites is known as a function of time (see Eq. (3) in [Luo and Toppoto \(2015\)](#)).

2.3. Initial conditions

Ballistic capture orbits are subdivided into two legs, namely, pre- and post-capture orbits. The patching point is the point of first closest passage. This is the initial condition in our simulations. The whole orbit is achieved by patching together the forward and backward integrations. The initial conditions are defined in RTN@ t_0 ,

which is a **inertial** frame. Integrating the motion in this frame allows us 1) tracking the authentic number of revolutions (so avoiding discrepancies with the rotating frame), 2) computing conveniently the Kepler energy, and 3) inferring direct geometrical interpretations on the capture dynamics.

In principle, six numbers have to be assigned to define an initial condition to integrate under Eqs. (1). The set used is made of orbital elements defined at the initial time t_0 : periapsis radius r_0 , eccentricity e_0 , inclination i_0 , right ascension of the ascending node Ω_0 , argument of periapsis ω_0 , and true anomaly f_0 . In practice, we fix $f_0 = 0$ and **assume** $e_0 \in [0.9, 1)$. That is, the initial condition **lies at** the periapsis of a highly eccentric osculating ellipse. **The latter feature favors escape in backward time and planet close passages in forward time (see Section 3.2)**. This is consistent with **Hyeraci and Topputo (2010)** and later works by the authors. **Stable sets for lower eccentricity are given in Topputo and Belbruno (2009)**. The initial inclination and orientation of the osculating plane is also fixed by assigning i_0 and Ω_0 , respectively. **A comprehensive analysis with varying initial inclination and orientation is presented in Luo and Topputo (2015)**. The remaining two parameters, r_0 and ω_0 , are discretized into N_{r_0} and N_{ω_0} points, respectively. The computational grid is then made of $N_{ic} = N_{r_0} \times N_{\omega_0}$ initial conditions; see **Luo et al. (2014)**.

2.4. Numerical integration

The initial orbital elements are converted into position and velocity vectors, \mathbf{r}_0 and \mathbf{v}_0 , respectively, in the RTN@ t_0 frame. Let $\mathbf{x}(t_0) = (\mathbf{r}_0, \mathbf{v}_0)$ be the initial state. This is flown under Eqs. (1) until a specific stop condition is verified (see Section 3.1). Let the terminal state be $\mathbf{x}(t) = (\mathbf{r}(t), \mathbf{v}(t))$, where $t \in [t_0, t_0 \pm T]$, the plus/minus signs account for forward/backward integrations, whereas T is a maximum time duration. A 7th/8th order Runge–Kutta–Fehlberg integrator is used with absolute and relative tolerances set to 10^{-12} . The equations of motion are scaled for numerical consistency. The gravitational, length, time, and speed units are $\text{MU} = Gm_p$, $\text{LU} = R$, $\text{TU} = (\text{LU}^3/\text{MU})^{1/2}$, and $\text{VU} = \text{LU}/\text{TU}$, respectively.

3. Methodology

The way ballistic capture orbits are constructed is given in this section; this is similar to Section 3 in **Luo and Topputo (2015)** with proper specializations to consider the presence of the moons. We have used the algorithm in **Luo et al. (2014)**; the reader can consult these two references for further details.

3.1. Classification of orbits

The particle motion is classified according to geometrical and energetic criteria. To this aim, a semi-plane is introduced to count the revolutions of the particle around the planet (dark grey plane in Fig. 2(a)). Let \mathbf{r}_0 and \mathbf{v}_0 be the particle initial position and velocity, respectively, in EME2000 centered at the planet. These are obtained by conversion of the initial orbital elements given in the computational grid, see Section 2.3. Let also $\mathbf{r}(t)$ and $\mathbf{v}(t)$ be the same quantities at a subsequent (or previous) time t ; $\mathbf{h}_0 = \mathbf{r}_0 \times \mathbf{v}_0$ is the initial angular momentum. The particle lies on the intersection plane if $\mathbf{r}(t) \cdot (\mathbf{h}_0 \times \mathbf{r}_0) = 0$.

Remark 1 (Revolution). *The particle performs a complete revolution around the planet at time t_1 if the following conditions are all simultaneously satisfied,*

$$\mathbf{r}^{(i)}(t_1) \cdot (\mathbf{h}_0 \times \mathbf{r}_0) = 0, \quad \mathbf{r}^{(i)}(t_1) \cdot \mathbf{r}_0 > 0, \quad (\mathbf{v}^{(i)}(t_1) \cdot \mathbf{v}_0) (\mathbf{v}^{(i-1)} \cdot \mathbf{v}_0) > 0, \quad (2)$$

where the superscript (i) counts the number of orbit-plane intersections.

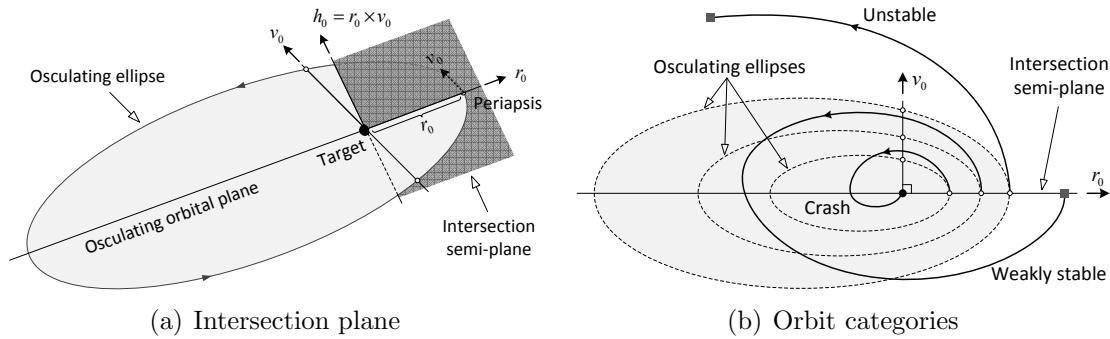


Figure 2: Classification of orbits behavior.

The **dimensionless** Kepler energy of the particle with respect to the planet is

$$H(t) = \frac{v^2(t)}{2} - \frac{1}{r(t)}, \quad (3)$$

where $r(t) = \|\mathbf{r}(t)\|$ and $v(t) = \|\mathbf{v}(t)\|$. $H(t)$ is not constant due to third-body perturbations; its sign indicates which body dominates over the particle trajectory.

Remark 2 (Escape). *The particle escapes from the planet at time t_e if the following two conditions are simultaneously satisfied,*

$$H(t_e) > 0, \quad r(t_e) > R_s, \quad (4)$$

where R_s is the radius of the planet sphere of influence (see Table 1).

The two conditions in (4) have to be satisfied simultaneously because the first one alone does not guarantee escape, and vice versa (Sousa Silva and Terra, 2012). Impacts occur at time t_i when $r(t_i) \leq R$, with R as in Table 1. Given \mathbf{r}_0 , \mathbf{v}_0 and an initial epoch t_0 , the particle motion is integrated forward under Eqs. (1). Orbits are classified into five different categories (see Fig. 2(b)).

Remark 3 (Classification). *The following sets of initial conditions (i.c.) are constructed according to the orbits they generate.*

- 1) *Weakly Stable Set, \mathcal{W}_1 : Contains i.c. whose orbits perform a complete revolution about the planet without escaping from or impacting with it (see Fig. 3(a)).*
- 2) *Unstable Set, \mathcal{X}_1 : Contains i.c. whose orbits escape from the planet without completing any revolution around it (see Fig. 3(b)).*
- 3) *Crash Set, \mathcal{K}_1 : Contains i.c. whose orbits impact with the planet without completing any revolution around it (see Fig. 3(c)).*
- 4) *Moon crash Set, \mathcal{M}_1 : Contains i.c. whose orbits impact with one of the moons without completing any revolution around the planet (see Fig. 3(d)).*
- 5) *Acrobatic Set, \mathcal{D}_1 : Contains i.c. with orbits not satisfying the above conditions within a given time span of $T = 8\pi(R_s)^{3/2}$ (see Fig. 3(e)).*

3.2. Construction of ballistic capture orbits

The classification in Remark 3 can be applied to orbits performing n revolutions forward in time, $n \geq 1$, and therefore the sets \mathcal{W}_n , \mathcal{X}_n , \mathcal{K}_n , \mathcal{M}_n , and \mathcal{D}_n can be defined starting from \mathcal{W}_{n-1} . Moreover, performing a backward integration yields \mathcal{W}_{-1} , \mathcal{X}_{-1} , \mathcal{K}_{-1} , \mathcal{M}_{-1} , and \mathcal{D}_{-1} . The capture set, a set containing initial conditions that generate ballistic capture orbits, is

$$\mathcal{C}_{-1}^n = \mathcal{X}_{-1} \cap \mathcal{W}_n. \quad (5)$$

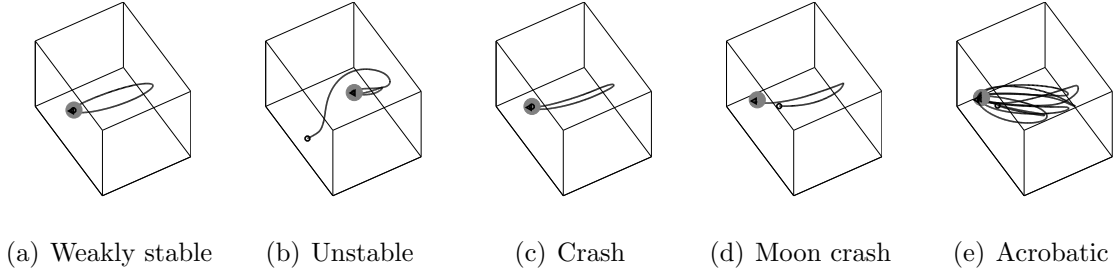


Figure 3: Sample orbits in the RTN@ t_0 frame. The grey spot is the Earth (not to scale).

The initial condition in \mathcal{C}_{-1}^n give rise to orbits that 1) escape the planet in backward time (\mathcal{X}_{-1} part), or equivalently approach it in forward time from outside of the SOI, and 2) perform at least n revolutions about the planet (\mathcal{W}_n part). The backward and forward orbits are linked at t_0 where they share the initial state **given** by the osculating orbital parameters defined on the computational grid. **Note that the generic capture set might be defined as $\mathcal{C}_{-m}^n = \mathcal{X}_{-m} \cap \mathcal{W}_n$. The choice $m = 1$ in (5) is driven by the fact that orbits immediately escaping the planet in backward time (without orbiting it) are sought. All subsequent forward revolutions are considered in \mathcal{W}_n . This stems from the analysis in Hyeraci and Topputo (2010).**

3.3. Ranking candidate orbits

The capture set defined in (5) contains a number of points that depend upon the discretization used to compute \mathcal{W}_n and \mathcal{X}_{-1} . A fine discretization is usually favored not to lose possible interesting dynamics, although the majority of \mathcal{C}_{-1}^n is made of spurious, useless solutions. This in turn raises the issue of finding criteria for the selection of the most interesting dynamics, **in order to avoid** scanning the whole capture set manually.

In the context of this work, the focus is on those orbits whose dynamics show a sudden change when going from the pre-capture to the post-capture phase. The pair (t_0, \mathbf{x}_0) is used to indicate the initial time and state, the latter being the periapsis of the initial osculating ellipse.

Remark 4 (Pre- and post-capture). *The ballistic capture orbits in \mathcal{C}_{-1}^n are subdivided in two portions, namely*

- i) Pre-capture (\mathcal{X}_{-1} part in \mathcal{C}_{-1}^n): Is the portion of orbit ranging from (t_0, \mathbf{x}_0) to $(t_{-1}, \mathbf{x}_{-1})$, $t_{-1} < t_0$, where the escape conditions are verified (see Remark 2).*

ii) *Post-capture (\mathcal{W}_n part in \mathcal{C}_{-1}^n): Is the portion of orbit ranging from (t_0, \mathbf{x}_0) to (t_n, \mathbf{x}_n) , $t_n > t_0$, where the n -turn condition is verified (see Remark 1).*

The aim is finding orbits having a) the highest energy when approaching the planet (pre-capture portion) and b) the most regular path after the first close encounter (post-capture portion). In the formalism of the patched-conics method, the pre-capture has to occur in a fashion resembling an incoming hyperbola, whereas the post-capture has to show a repetitive, regular behavior, typical of a two-body ellipse. Note that this dichotomy is sought by simply exploiting the natural dynamics: no orbital maneuvers are admitted. Ideally, *we want to turn an hyperbola into an ellipse on a zero-cost basis.*

The feature in point a) is desirable because increasing the approaching energy yields a reduction of the heliocentric duration to rendezvous with the planet (Macdonald and McInnes, 2005). A highly energetic approach that turns into a ballistic capture orbit enforces the multi-body system to work at its maximum capability to slow down the particle and trap it about the planet. The following indicator is used to measure the energy of the approaching particle,

$$C_3 = v_\infty^2, \quad (6)$$

where v_∞ is the velocity measured at the planet SOI (see Table 1).

The requirement in point b) sets the post-capture orbit to behave regularly. A post-capture repetitive geometry is twofold: it can allow similar, multiple insertion options into a more stable orbit, and it is suitable to analyze the mission performances in case the ballistic capture orbit is baselined as definitive orbit. The capture regularity is measured through the stability index

$$\mathcal{S} = \frac{t_n - t_0}{n} \quad (7)$$

where n is the number of revolutions completed by the particle. In Luo et al. (2014); Luo and Topputo (2015) it has been shown that low values of \mathcal{S} are associated to regular post-capture orbits.

Remark 5 (Ideal orbits). *Ideal orbits are orbits in \mathcal{C}_{-1}^n having high C_3 and low \mathcal{S} .*

The two conditions imposed to ideal orbits are in antithesis. It is natural that increasing C_3 yields to either planet fly-by orbits (no capture) or irregular post-capture dynamics, and thus to high \mathcal{S} . For this reason, ideal orbits are viewed as those solutions belonging to the Pareto frontier in a (C_3, \mathcal{S}) plane.

Figure 4 shows the solutions belonging to \mathcal{C}_{-1}^6 about the Earth projected on the (C_3, \mathcal{S}) plane. For this case, two simulations have been carried out, and two different solution sets have been computed: the set M_1 , which considers the Moon (grey dots), and the set M_2 , where the Moon is neglected (red squares). This distinction is necessary to assess the capability of the Moon in enabling or improving the capture at the Earth. Sample Pareto-optimal solutions are labelled (A_1, \dots, F_1 and A_2, \dots, F_2 , belonging to M_1 and M_2 , respectively) to ease the discussion (see Section 4.1). Orbits of practical interest can be picked from the Pareto-optimal points depending on the mission requirements. A summary of the developed algorithm to construct ballistic capture orbits and to select the ideal ones is outlined in Fig. 5.

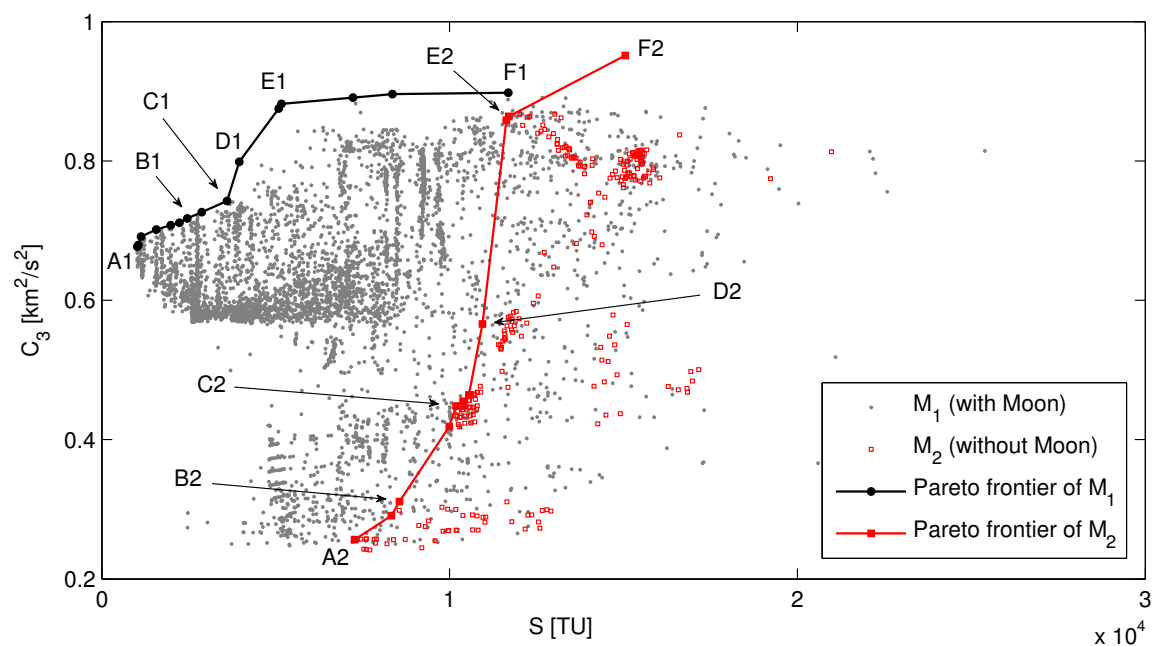


Figure 4: Solutions in \mathcal{C}_{-1}^6 about the Earth (sets M_1 and M_2) and their Pareto frontiers.

4. Case Studies

In this section we analyze two cases involving ballistic capture about the Earth and Jupiter. In both cases the set \mathcal{C}_{-1}^6 is considered. This is consistent with real applications (Jehn et al., 2004) and allows us comparing the results with previous works (Hyaraci and Topputo, 2010; Luo et al., 2014; Luo and Topputo, 2015). The aim is investigating the influence of the Moon and that of the Galilean moons. The

- 1) **Initialization**
 - Select initial epoch t_0 , Sun, planet, and its satellites involved (Table 1)
 - Set forward revolution number (n) and backward number (-1)
 - Set orbital elements at t_0 for the Sun and the satellites
 - Set initial eccentricity ($e_0 \in [0.9, 1)$), inclination ($i_0 \in [0, \pi]$), and RAAN ($\Omega_0 \in [0, 2\pi)$)
 - Discretize periapsis distance, $r_0 \in [R + \epsilon, R_s]$, and argument of periapsis, $\omega_0 \in [0, 2\pi)$
 - Set maximum integration time T
 - Normalize all variables
- 2) **Computation**
 - Assign $j =$ current revolution number
 - IF $|j| = 1$
 - a) Extract current value of r_0 and ω_0
 - b) Transform $(t_0, r_0, e_0, i_0, \Omega_0, \omega_0, f_0 = 0)$ to Cartesian state (t_0, \mathbf{x}_0) in RTN@ t_0
 - c) Forward ($j = 1$)/backward ($j = -1$) integrate (t_0, \mathbf{x}_0)
 - d) Stop when one of the five conditions in Remark 3 is verified (see Fig. 3)
 - e) Classify the initial conditions and assign them to $\mathcal{W}_j, \mathcal{X}_j, \mathcal{K}_j, \mathcal{M}_j, \mathcal{D}_j$
 - ELSEIF $2 \leq j \leq n$
 - a) Forward integrate the terminal state in \mathcal{W}_{j-1}
 - b) Stop when one of the five conditions in Remark 3 is verified (see Fig. 3)
 - c) Classify the initial conditions and assign them to $\mathcal{W}_j, \mathcal{X}_j, \mathcal{K}_j, \mathcal{M}_j, \mathcal{D}_j$
 - END
- 3) **Manipulation**
 - Extract \mathcal{C}_{-1}^n by intersecting \mathcal{W}_n and \mathcal{X}_{-1} as per Eq. (5)
- 4) **Representation**
 - Reconstruct ballistic capture solutions in \mathcal{C}_{-1}^n within $[t_{-1}, t_n]$
 - Calculate C_3 and \mathcal{S} with Eq. (6) and (7), respectively
 - Compute Kepler energy ($H(t)$ in (3)) and altitude profiles
 - Check approaching direction
 - Check overall orbit geometry (osculating plane, close passages, etc.)
 - Project solutions in the (C_3, \mathcal{S}) plane, and compute the Pareto frontier
 - Select sample Pareto-optimal solutions matching mission requirements (e.g., C_3 given)
 - Validate selected trajectories in a full ephemeris model

Figure 5: Outline of the algorithm developed.

capability of these natural satellites in improving the ballistic capture is measured quantitatively and assessed qualitatively. The settings are those in Table 1.

4.1. Ballistic Capture at the Earth

The set up for this case is as follows (refer to Section 2.3 for the definition and meaning of the parameters). 1) $t_0 = 2458888.82$ JD (or 9 February 2020); at this epoch, the Sun and the Moon are in opposition with respect to the Earth (i.e.,

$\theta_{1,0} = 0$ and $\theta_{s,0} = \pi$ in Fig. 1). 2) $e_0 = 0.95$; this eases comparisons with previous works (Luo et al., 2014). 3) $i_0 = 22.5$ deg and $\Omega_0 = 225$ deg; this specifies the plane on which initial conditions lie. 4) r_0 and ω_0 are uniformly discretized into $N_{r_0} = 919$ and $N_{\omega_0} = 720$ points, respectively, and thus the computational grid is made of $N_{ic} = 661,680$ initial conditions; the bounds for r_0 and ω_0 are given in Fig. 5 ($\epsilon = 1$ km). 5) $n = 6$, that is, we are looking for post-capture orbits that perform at least six revolutions about the Earth. 6) The model in Eq. (1) considers the gravitational attractions of the Earth, the Sun, and the Moon; this is chosen to limit the computational burden while still retaining high-fidelity solutions.

Fig. 6 shows the sets of initial conditions \mathcal{W}_1 , \mathcal{W}_6 , \mathcal{W}_{-1} , and \mathcal{C}_{-1}^6 projected in the $(r_0 \cos \omega_0, r_0 \sin \omega_0)$ plane. The points are coloured depending on their stability index, \mathcal{S} , defined in Eq. (7), which is reported on the side bars. For the analysis below, it is worth mentioning that lower values of \mathcal{S} lead to regular post-capture orbits, which is desirable.

By inspecting Fig. 6 it can be seen that all the sets present an anomaly at $\omega_0 \simeq 135$ deg. This is ascribable to the presence of the Moon (recall that $\Omega_0 = 225$ deg and $\theta_{1,0} = 0$, see Fig. 1). This feature is a departure from previously computed sets where the stable and capture sets present two symmetrical branches (Topputo and Belbruno, 2009; Hyeraci and Topputo, 2010; Luo et al., 2014; Luo and Topputo, 2015). Moreover, it is interesting to notice that in \mathcal{C}_{-1}^6 , or the set from which practical solutions are extracted, the points with lower \mathcal{S} aggregate about the anomaly at $\omega_0 = 135$ deg. The upper-left branch is also wider than the lower-right one. There is evidence that the presence of the Moon favours capturing orbits that would not do so without the Moon (larger branch), and improves the quality of the post-capture dynamics (lower \mathcal{S}).

The role played by the Moon is also assessed by comparing the set M_1 (with Moon) and M_2 (without Moon) in Fig. 4. The points in Fig. 4 have been obtained with exactly the same settings in terms of initial conditions except that the model in Eq. (1) considers the Moon (M_1) or not (M_2). It can be seen that in general, the solutions in M_1 are more numerous than those in M_2 , which indicates that the presence of the Moon increases the chances of capture. Most importantly, when going from model M_2 to M_1 , the Pareto frontier of M_2 (red line) is moved to the upper-left part of the plot. This proves the benign effect of the Moon in ballistic capture orbits: it yields lower \mathcal{S} and higher C_3 , which is ideal.

Six sample solutions belonging to the two Pareto frontiers of M_1 and M_2 , indicated in Fig. 4, are analyzed in Table 2. For each solution, the coordinates in the (C_3, \mathcal{S}) plane are reported, and the orbit in the BPR frame is also shown. Dramatic improvements on both hyperbolic excess velocity and post-capture stability

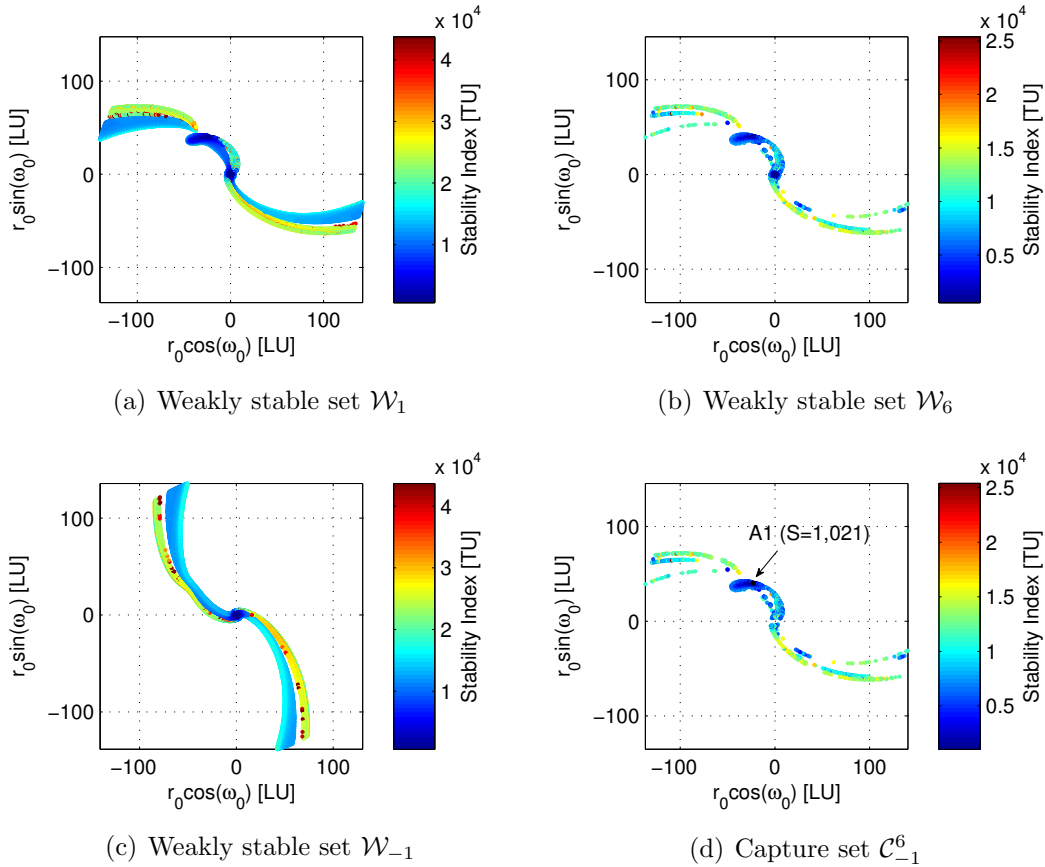






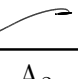
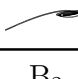

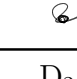
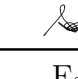
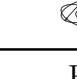








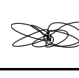
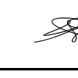
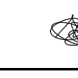
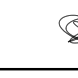


Figure 6: Forward and backward weakly stable sets and capture set about the Earth. Points are coloured depending on their stability index (reported in the side bar). The solution A_1 in C_{-1}^6 is the Pareto-optimal point in Fig. 4 with the lowest value of \mathcal{S} among all the solutions found.

are obtained when the orbits are allowed to exploit the presence of the Moon. For instance, comparing A_2 against A_1 (solutions with lowest \mathcal{S} in the sets they belong to), the average post-capture period decreases from approximately 68 days to 10 days, whereas the hyperbolic excess velocity increases from approximately 500 m/s ($C_3 = 0.256 \text{ km}^2/\text{s}^2$) to 820 m/s ($C_3 = 0.677 \text{ km}^2/\text{s}^2$). This is a major improvement, and can be also inferred by looking at the orbits shape in Table 2.

Solution A_1 (indicated in Fig. 4 and 6(d)) is now analyzed. Among the orbits simulated in this case study, this is the solution with lowest stability index ($\mathcal{S} = 1021$ TU) and thus it belongs to the Pareto frontier by definition (see Fig. 4). The orbit generated by forward and backward integration of the initial condition associated to

Table 2: Feature of sample solutions belonging to the Pareto frontiers of M_1 and M_2 (Earth case).

Solution	A ₁	B ₁	C ₁	D ₁	E ₁	F ₁
C_3 (km ² /s ²)	0.677	0.718	0.742	0.799	0.882	0.898
\mathcal{S} (days)	9.534	22.981	33.645	36.951	48.222	109.237
(x, y) , BPR						
(x, z) , BPR						
Solution	A ₂	B ₂	C ₂	D ₂	E ₂	F ₂
C_3 (km ² /s ²)	0.256	0.311	0.448	0.566	0.864	0.951
\mathcal{S} (days)	67.916	79.925	95.146	102.220	109.289	140.564
(x, y) , BPR						
(x, z) , BPR						

A_1 is shown in Fig. 7 in the RTN@ t_0 frame centered at the Earth. The initial position of the Sun, the Moon, and the particle is indicated with the triangular marker. It can be seen that the post-capture orbit ($t > t_0$) experiences a fly-by at the Moon. After such close encounter, the orbit evolves in a regular fashion resembling a two-body dynamics. This was expected, A_1 being the solution with lowest stability index. This process can be inferred by looking at the histories of the Kepler energy with respect to the Earth and the distances to the Earth and Moon, as shown in Fig. 8. The closest altitude to the Moon is at 746 km. After this, the post-capture orbit becomes extremely regular and stable, akin to a cislunar transfer orbit (see close-up in Fig. 7(b)). By definition, the Kepler energy with respect to the Earth is negative in the post-capture portion. The pre-capture orbit ($t < t_0$) escapes the Earth in backward time, as expected. It is interesting to notice that solution A_1 is not isolated, but rather it belongs to a cluster of points in \mathcal{C}_{-1}^6 ; see Fig. 6(d). In case this solution is baselined in applied scenarios and, for some reason, an accurate targeting is not possible, the region about it will still assure capture, so increasing the strategy robustness.

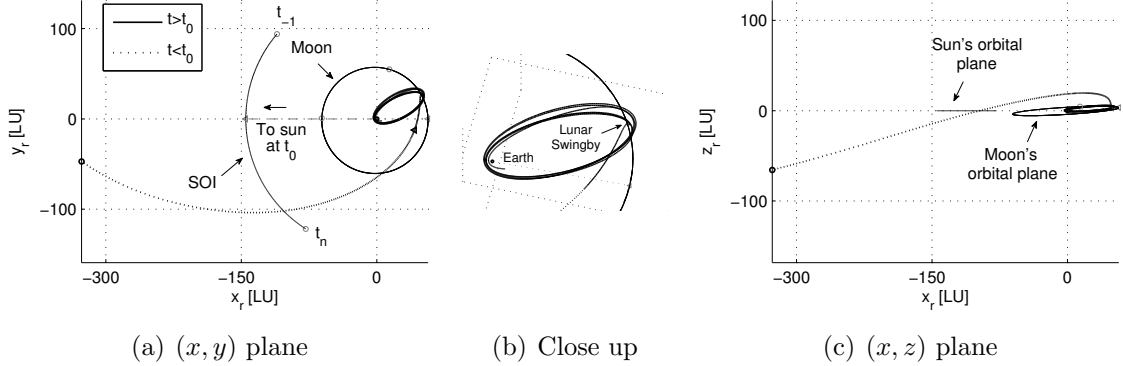


Figure 7: Orbit corresponding to solution A_1 (Earth case) in the RTN@ t_0 frame.

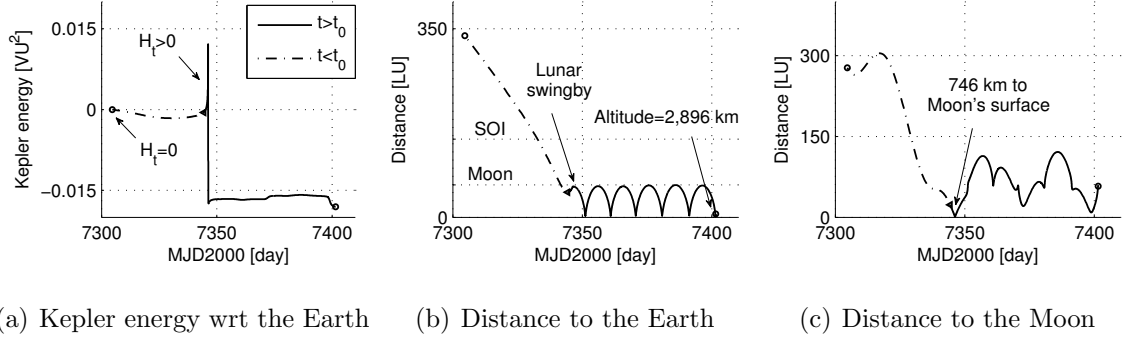


Figure 8: Parameter histories of solution A_1 .

4.2. Ballistic Capture at Jupiter

Ballistic capture orbits that interact with multiple natural satellites are studied in the Jovian system. In this case, the gravitational attractions of the Sun, Jupiter, and the four Galilean satellites (Io, Europa, Ganymede, and Callisto) are considered in Eq. (1). Beside the parameters in Table 1, the other variables have been set as follows. 1) $t_0 = 2459965.00$ JD (20 January 2023), when Jupiter is at the perihelion; this condition maximizes the chances of having capture orbits, as discussed in [Circi \(2012\)](#); [Hyeraci and Topputo \(2013\)](#); [Luo and Topputo \(2015\)](#). 2) $e_0 = 0.95$, as in the previous case. 3) $i_0 = 0$ deg (and thus Ω_0 is not defined); this maximizes the probability of encountering the moons (see the obliquities in Table 1); 4) ω_0 is uniformly discretized into $N_{\omega_0} = 720$ points, whereas r_0 is defined on a nonuniform

grid: the grid is finer in the region close to Jupiter (519 points in $[R + \epsilon, 30R]$ ³ and coarser in the rest of the space (922 points in $[30R, R_s]$); in total, $N_{ic} = 1,037,520$ initial conditions are analyzed; 5) $n = 6$, as in the previous case.

Fig. 9 presents the capture set \mathcal{C}_{-1}^6 and a close up to its inner portion in the $(r_0 \cos \omega_0, r_0 \sin \omega_0)$ plane. By comparing Fig. 9 against Fig. 6, it can be seen that the capture set at Jupiter is more scattered and less regular than that at the Earth. These features are not found in moon-free models (Topputo and Belbruno, 2009; Romagnoli and Circi, 2009; Makó et al., 2010), and thus there is evidence that it is caused by the multiple interactions with the moons, which give rise to a lesser smooth vector field. Moreover, the solutions with the lowest stability index (i.e., those of practical interest) are aggregated about the region near Jupiter.

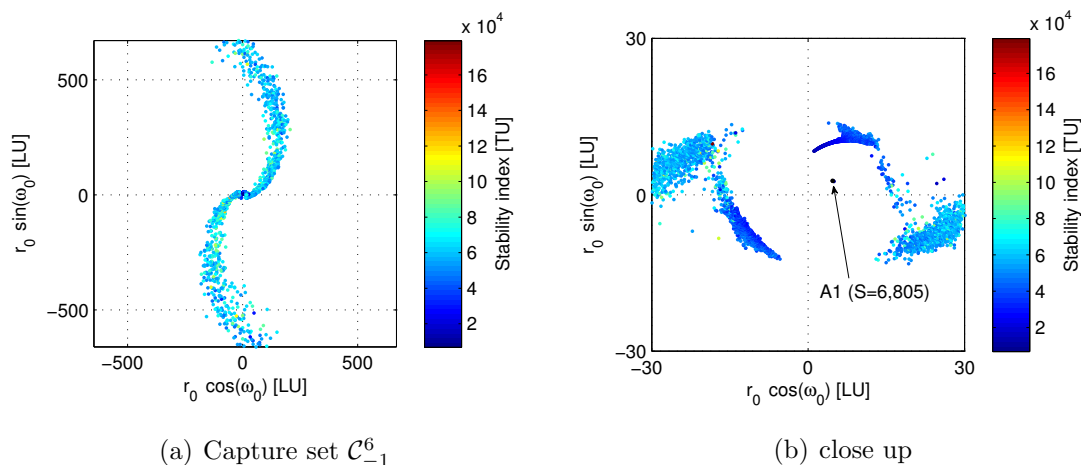


Figure 9: Capture set \mathcal{C}_{-1}^6 about Jupiter. The points are coloured according to their stability index, reported in the side bar. A_1 is the solution with the minimum \mathcal{S} .

It is interesting to view the solutions belonging to \mathcal{C}_{-1}^6 in the (C_3, \mathcal{S}) plane. The initial conditions defined on the computational grid have been reintegrated in an artificial, moon-free model (labelled M_2), and assessed against those accounting for the Galilean satellites (M_1 model). Figure 10 summarizes the outcome of this exercise. The solutions in \mathcal{C}_{-1}^6 obtained in the M_1 model are more numerous than those in the M_2 model, so confirming once again that the presence of the natural satellites improves the chances of achieving the capture. Most importantly, the point in M_1 involve lower stability index \mathcal{S} and higher pre-capture energy C_3 . This is remarkable.

³Note that the semi-major axis of Callisto's orbit around Jupiter is 26.22 Jupiter radii.

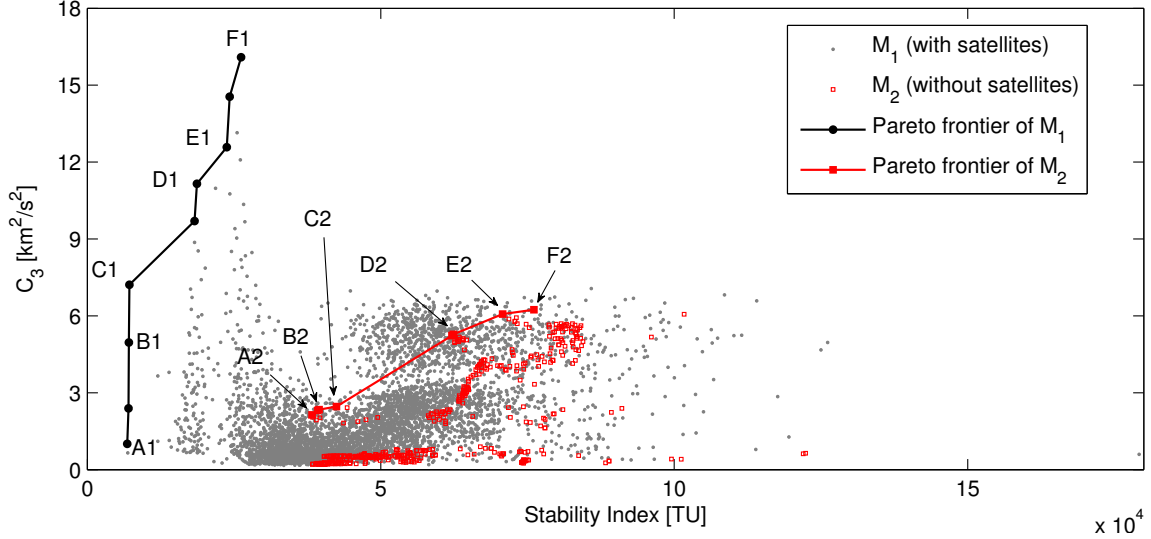














Figure 10: Solutions in C_{-1}^6 about Jupiter (sets M_1 and M_2) and their Pareto frontiers.

Samples solutions belonging to the two Pareto frontiers of M_1 and M_2 in Fig. 10 are detailed in Table 3. Beside C_3 and \mathcal{S} , for the points in M_1 , the flyby moon and the minimum altitude relative to it are also given. The associated orbits projected in the (x, y) plane (BPR frame) are also provided; the out-of-plane motion is negligible. Notice the low altitudes of solutions D_1 and F_1 with respect to Ganymede, which may eventually lead to discard them in practical application. (This assessment is however out of the scopes of this work.)

We note from Table 3 that $v_\infty \simeq 4$ km/s ($C_3 = 16.089$ km²/s²) in solution F_1 is consistent with the result in Macdonald and McInnes (2005). The hyperbolic excess velocity could be further increased by exploiting multiple lunar fly-byes (Landau et al., 2010). This would also generate a more refined Pareto frontier. However, solutions of this kind have to be imposed explicitly when designing Jupiter multi-moon tours. This can be done, for instance, by studying the post-capture orbit with the Tisserand-Poincaré graph and Laplace resonances (Campagnola et al., 2014; Kloster et al., 2011), and patching it with a consistent pre-capture orbit. In this work, multiple flybys are not imposed, because the focus is to assess the impact of the natural satellites on the capture sets. In our solutions, capture orbits about Jupiter exist even when moons are not exploited (see solutions A_2, \dots, F_2 in Table 3), by virtue of the simultaneous gravitational attraction of the Sun and Jupiter upon the massless particle. This is not the case of orbits designed with a patched-conics method.

Table 3: Feature of sample solutions belonging to the Pareto frontiers of M_1 and M_2 (Jupiter case); h_{\min} is the minimum altitude to the flyby satellite.

Solution	A ₁	B ₁	C ₁	D ₁	E ₁	F ₁
C_3 (km ² /s ²)	1.004	4.961	7.210	11.161	12.580	16.089
\mathcal{S} (days)	133.763	139.168	140.780	367.381	467.039	515.001
Flyby moon	Io	Io	Io	Gan.	Gan.	Gan.
h_{\min}	452.601	473.357	105.888	52.610	814.000	51.135
(x, y) , BPR						
Solution	A ₂	B ₂	C ₂	D ₂	E ₂	F ₂
C_3 (km ² /s ²)	2.138	2.339	2.459	5.281	6.067	6.241
\mathcal{S} (days)	752.846	776.040	834.420	1,225	1,391	1,495
(x, z) , BPR						

The orbit corresponding to solution C_1 in Table 3, which has a good balance between C_3 and \mathcal{S} (see Fig. 10), is shown in Fig. 11. The close up shows that the spacecraft passes by the satellite Io before its first periapsis to Jupiter (during the pre-capture leg). Further features can be seen in Fig. 12. After the flyby, the spacecraft moves along an elongated, regular orbit with a periapsis distance less than Io's semi-major axis about Jupiter and an apoapsis at about 200 Jupiter radii. The post-capture orbit is occasionally perturbed by the gravity of Io (see Fig. 12(a)).

5. Conclusions

In this paper, the capability of natural satellites of improving the ballistic capture performances has been explored. This is done by taking into account the presence of moons in a previously developed method. In this model, a computational grid of initial conditions is defined, and orbits are classified according to a simple definition of stability. A proper manipulation of the resulting sets allows us to find ballistic capture orbits with prescribed stability number. Two indicators, namely the excess velocity and the stability index, are used to judge the performance of pre- and post-

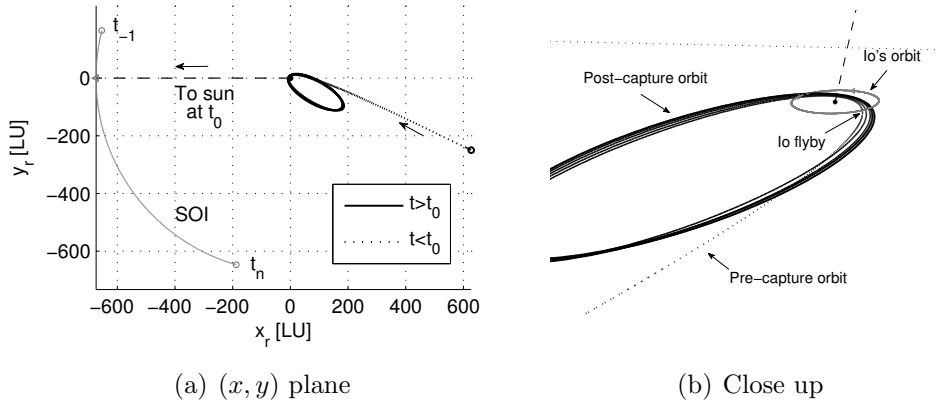


Figure 11: Orbit corresponding to solution C_1 (Jupiter case) in the $RTN@t_0$ frame..

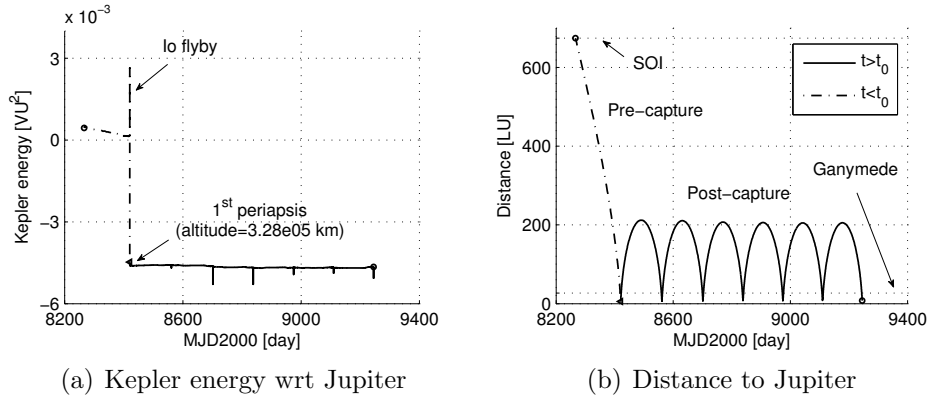


Figure 12: Parameter histories of solution C_1 .

capture legs. Pareto optimality is used to extract solutions having the best balance of pre-capture energy and post-capture regularity.

Numerical simulations have been performed for two case studies relevant for applications: Earth and Jupiter. In both cases, results have shown that the presence of the moons increases the chances of performing ballistic capture about the planet, improves the regularity of the post-capture orbit, and may accommodate higher pre-capture energies than a moon-free model. **Although** exploiting the moons to improve capture might be a powerful option, the presented method supports ballistic capture in no-moon scenarios as well.

Acknowledgements

Z.-F. Luo acknowledges financial support from China Scholarship Council, the Innovation Fund of National University of Defense Technology (Grant No. B100101) and the National Natural Science Foundation of China (Grant No. 11602301).

References

- Alessi, E.M., Gómez, G., Masdemont, J.J., 2012. Further advances on low-energy lunar impact dynamics. *Communications in Nonlinear Science and Numerical Simulation* 17, 854–866. doi:[10.1016/j.cnsns.2011.06.037](https://doi.org/10.1016/j.cnsns.2011.06.037).
- Astakhov, S.A., Burbanks, A.D., Wiggins, S., Farrelly, D., 2003. Chaos-assisted capture of irregular moons. *Nature* 423, 264–267. doi:[10.1038/nature01622](https://doi.org/10.1038/nature01622).
- Belbruno, E., 2004. *Capture Dynamics and Chaotic Motions in Celestial Mechanics: With Applications to the Construction of Low Energy Transfers*. Princeton University Press.
- Belbruno, E., Miller, J., 1993. Sun-perturbed Earth-to-Moon transfers with ballistic capture. *Journal of Guidance, Control, and Dynamics* 16, 770–775. doi:[10.2514/3.21079](https://doi.org/10.2514/3.21079).
- Belbruno, E., Moro-Martín, A., Malhotra, R., Savransky, D., 2012. Chaotic exchange of solid material between planetary systems: Implications for lithopanspermia. *Astrobiology* 12, 754–774. doi:[10.1089/ast.2012.0825](https://doi.org/10.1089/ast.2012.0825).
- Benner, L.A., McKinnon, W.B., 1995. On the orbital evolution and origin of comet Shoemaker–Levy 9. *Icarus* 118, 155–168. doi:[10.1006/icar.1995.1182](https://doi.org/10.1006/icar.1995.1182).
- Brasil, P., Prado, A., Deienno, R., Yokoyama, T., 2015. Study of the gravitational capture of a spacecraft by Jupiter. *Advances in Space Research* 55, 668–681. doi:[10.1016/j.asr.2014.11.005](https://doi.org/10.1016/j.asr.2014.11.005).
- Brunini, A., 1996. On the satellite capture problem: capture and stability regions for planetary satellites. *Celestial Mechanics and Dynamical Astronomy* 64, 79–92. doi:[10.1007/978-94-009-0307-4_7](https://doi.org/10.1007/978-94-009-0307-4_7).
- Campagnola, S., Buffington, B., Petropoulos, A., 2014. Jovian tour design for orbiter and lander missions to Europa. *Acta Astronautica* 100, 68–81. doi:[10.1016/j.actaastro.2014.02.005](https://doi.org/10.1016/j.actaastro.2014.02.005).

- Circi, C., 2012. Properties of transit trajectory in the restricted three and four-body problem. *Advances in Space Research* 49, 1506–1519. doi:[10.1016/j.asr.2012.02.034](https://doi.org/10.1016/j.asr.2012.02.034).
- Circi, C., Teofilatto, P., 2001. On the dynamics of weak stability boundary lunar transfers. *Celestial Mechanics and Dynamical Astronomy* 79, 41–72. doi:[10.1023/A:1011153610564](https://doi.org/10.1023/A:1011153610564).
- Cline, J.K., 1979. Satellite aided capture. *Celestial Mechanics* 19, 405–415. doi:[10.1007/BF01231017](https://doi.org/10.1007/BF01231017).
- Conley, C.C., 1968. Low energy transit orbits in the restricted three-body problem. *SIAM Journal on Applied Mathematics* 16, 732–746. doi:[10.1137/0116060](https://doi.org/10.1137/0116060).
- García, F., Gómez, G., 2007. A note on weak stability boundaries. *Celestial Mechanics and Dynamical Astronomy* 97, 87–100. doi:[10.1007/s10569-006-9053-6](https://doi.org/10.1007/s10569-006-9053-6).
- Hyeraci, N., Topputo, F., 2010. Method to design ballistic capture in the elliptic restricted three-body problem. *Journal of Guidance, Control, and Dynamics* 33, 1814–1823. doi:[10.2514/1.49263](https://doi.org/10.2514/1.49263).
- Hyeraci, N., Topputo, F., 2013. The role of true anomaly in ballistic capture. *Celestial Mechanics and Dynamical Astronomy* 116, 175–193. doi:[10.1007/s10569-013-9481-z](https://doi.org/10.1007/s10569-013-9481-z).
- Ivashkin, V.V., 2002. On trajectories of Earth–Moon flight of a particle with its temporary capture by the Moon. *Doklady Physics* 47, 196–199. doi:[10.1134/1.1526433](https://doi.org/10.1134/1.1526433).
- Jehn, R., Campagnola, S., García, D., Kemble, S., 2004. Low-thrust approach and gravitational capture at Mercury, in: *Proceedings of the 18th International Symposium on Space Flights Dynamics*, Munich, Germany. pp. 487–492.
- Kary, D.M., Dones, L., 1996. Capture statistics of short-period comets: Implications for comet D/Shoemaker–Levy 9. *Icarus* 121, 207–224. doi:[10.1006/icar.1996.0082](https://doi.org/10.1006/icar.1996.0082).
- Kloster, K.W., Petropoulos, A.E., Longuski, J.M., 2011. Europa orbiter tour design with Io gravity assists. *Acta Astronautica* 68, 931–946. doi:[10.1016/j.actaastro.2010.08.041](https://doi.org/10.1016/j.actaastro.2010.08.041).

- Landau, D., Strange, N., Lam, T., 2010. Solar electric propulsion with satellite flyby for Jovian capture, Paper AAS-10-169, 20th AAS/AIAA Space Flight Mechanics Meeting, San Diego, California, 14–18 February, 2010.
- Luo, Z.F., Topputo, F., 2015. Analysis of ballistic capture in Sun-planet models. *Advances in Space Research* 56, 1030–1041. doi:[10.1016/j.asr.2015.05.042](https://doi.org/10.1016/j.asr.2015.05.042).
- Luo, Z.F., Topputo, F., Bernelli-Zazzera, F., Tang, G.J., 2014. Constructing ballistic capture orbits in the real Solar System model. *Celestial Mechanics and Dynamical Astronomy* 120, 433–450. doi:[10.1007/s10569-014-9580-5](https://doi.org/10.1007/s10569-014-9580-5).
- Lynam, A.E., Kloster, K.W., Longuski, J.M., 2011. Multiple-satellite-aided capture trajectories at Jupiter using the Laplace resonance. *Celestial Mechanics and Dynamical Astronomy* 109, 59–84. doi:[10.1007/s10569-010-9307-1](https://doi.org/10.1007/s10569-010-9307-1).
- Macdonald, M., McInnes, C.R., 2005. Spacecraft planetary capture using gravity-assist maneuvers. *Journal of Guidance, Control, and Dynamics* 28, 365–368. doi:[10.2514/1.11866](https://doi.org/10.2514/1.11866).
- Makó, Z., Szenkovits, F., Salamon, J., Oláh-Gál, R., 2010. Stable and unstable orbits around Mercury. *Celestial Mechanics and Dynamical Astronomy* 108, 357–370. doi:[10.1007/s10569-010-9309-z](https://doi.org/10.1007/s10569-010-9309-z).
- Mingotti, G., Topputo, F., Bernelli-Zazzera, F., 2012a. Efficient invariant-manifold, low-thrust planar trajectories to the Moon. *Communication in Nonlinear Science and Numerical Simulation* 17, 817–831. doi:[10.1016/j.cnsns.2011.06.033](https://doi.org/10.1016/j.cnsns.2011.06.033).
- Mingotti, G., Topputo, F., Bernelli-Zazzera, F., 2012b. Transfers to distant periodic orbits around the Moon via their invariant manifolds. *Acta Astronautica* 79, 20–32. doi:[10.1016/j.actaastro.2012.04.022](https://doi.org/10.1016/j.actaastro.2012.04.022).
- Parker, J.S., Born, G.H., 2008. Modeling a low-energy ballistic lunar transfer using dynamical systems theory. *Journal of Spacecraft and Rockets* 45, 1269–1281. doi:[10.2514/1.35262](https://doi.org/10.2514/1.35262).
- Ren, Y., Shan, J., 2014. Low-energy lunar transfers using spatial transit orbits. *Communications in Nonlinear Science and Numerical Simulation* 19, 554–569. doi:[10.1016/j.cnsns.2013.07.020](https://doi.org/10.1016/j.cnsns.2013.07.020).
- Romagnoli, D., Circi, C., 2009. Earth–Moon weak stability boundaries in the restricted three and four body problem. *Celestial Mechanics and Dynamical Astronomy* 103, 79–103. doi:[10.1007/s10569-008-9169-y](https://doi.org/10.1007/s10569-008-9169-y).

- Russell, R.P., Lam, T., 2007. Designing ephemeris capture trajectories at Europa using unstable periodic orbits. *Journal of Guidance, Control, and Dynamics* 30, 482–491. doi:[10.2514/1.22985](https://doi.org/10.2514/1.22985).
- Sousa Silva, P., Terra, M., 2012. Applicability and dynamical characterization of the associated sets of the algorithmic weak stability boundary in the lunar sphere of influence. *Celestial Mechanics and Dynamical Astronomy* 113, 141–168. doi:[10.1007/s10569-012-9409-z](https://doi.org/10.1007/s10569-012-9409-z).
- Topputo, F., Belbruno, E., 2009. Computation of weak stability boundaries: Sun–Jupiter system. *Celestial Mechanics and Dynamical Astronomy* 105, 3–17. doi:[10.1007/s10569-009-9222-5](https://doi.org/10.1007/s10569-009-9222-5).
- Topputo, F., Belbruno, E., 2015. Earth–Mars transfers with ballistic capture. *Celestial Mechanics and Dynamical Astronomy* 121, 329–346. doi:[10.1007/s10569-015-9605-8](https://doi.org/10.1007/s10569-015-9605-8).
- Tsui, K., 2000. Asteroid-planet-Sun interaction in the presence of a planetary satellite. *Icarus* 148, 139–146. doi:[10.1006/icar.2000.6475](https://doi.org/10.1006/icar.2000.6475).
- Yamato, H., Spencer, D., 2004. Transit-orbit search for planar restricted three-body problems with perturbations. *Journal of Guidance, Control, and Dynamics* 27, 1035–1045. doi:[10.2514/1.4524](https://doi.org/10.2514/1.4524).